

# ReManNet: A Riemannian Manifold Network for Monocular 3D Lane Detection

Chengzhi Hong    Bijun Li {Corresponding author}

State Key Laboratory of Information Engineering in Surveying, Mapping and Remote Sensing  
Wuhan University, Wuhan, China

ht005305@whu.edu.cn    lee@whu.edu.cn

## Abstract

*Monocular 3D lane detection remains challenging due to depth ambiguity and weak geometric constraints. Mainstream methods rely on depth guidance, BEV projection, and anchor- or curve-based heads with simplified physical assumptions, remapping high-dimensional image features while only weakly encoding road geometry. Lacking an invariant geometric-topological coupling between lanes and the underlying road surface, 2D-to-3D lifting is ill-posed and brittle, often degenerating into concavities, bulges, and twists. To address this, we propose the Road-Manifold Assumption: the road is a smooth 2D manifold in  $\mathbb{R}^3$ , lanes are embedded 1D submanifolds, and sampled lane points are dense observations, thereby coupling metric and topology across surfaces, curves, and point sets. Building on this, we propose ReManNet, which first produces initial lane predictions with an image backbone and detection heads, then encodes geometry as Riemannian Gaussian descriptors on the symmetric positive-definite (SPD) manifold, and fuses these descriptors with visual features through a lightweight gate to maintain coherent 3D reasoning. We also propose the 3D Tunnel Lane IoU (3D-TLIoU) loss, a joint point-curve objective that computes slice-wise overlap of tubular neighborhoods along each lane to improve shape-level alignment. Extensive experiments on standard benchmarks demonstrate that ReManNet achieves state-of-the-art (SOTA) or competitive results. On OpenLane, it improves F1 by +8.2% over the baseline and by +1.8% over the previous best, with scenario-level gains of up to +6.6%. The code will be publicly available at <https://github.com/changehome717/ReManNet>.*

## 1. Introduction

3D lane detection is a core perception task for autonomous driving because it provides metric lane geometry and semantics for downstream planning [24, 73], lane keeping [10, 29], and scene understanding [41, 76]. Although LiDAR offers reliable depth, its high cost and weak responses

on road markings limit large-scale deployment. In contrast, monocular cameras are inexpensive and capture rich appearance cues, motivating a shift toward monocular 3D lane detection. Nevertheless, recovering accurate lane geometry from a single image remains highly challenging without explicit depth supervision or principled geometric constraints.

Existing monocular 3D lane detectors can be broadly grouped into three categories. **(i) Depth-guided methods** [19, 38, 52, 68] infer depth or voxelized features before lifting image evidence into 3D, making performance sensitive to depth quality. **(ii) Bird’s-eye-view (BEV)-centric models** [9, 17, 18, 36] regress lanes from image-to-BEV features, but their implicit planarity assumptions can introduce systematic bias on nonplanar roads. **(iii) Line-modeling approaches** parameterize lanes using explicit anchors [20, 21, 75], polynomial curves [4, 5, 26, 51], or grouped keypoints [48, 63]. However, under challenging visual conditions, missing or corrupted local cues can lead to erroneous or incomplete point predictions, making the matching between detected lane evidence and the optimized line model unstable and thereby degrading overall accuracy.

Despite their different formulations, existing methods share a common design tendency: they prioritize 2D image features as the primary predictive signal, investing heavily in image-derived intermediate representations such as depth maps, BEV features, or planar reconstructions. By contrast, explicit 3D lane coordinates are relegated to an auxiliary role: as region-of-interest (RoI) sampling targets [20, 75], as supervision during training, and as weak geometric regularizers (e.g., parallelism [20, 21], smoothness [52], or projection of 3D structural priors into 2D [30]). This practice underutilizes 3D coordinates as carriers of metric constraints and topological structure. Lacking metric and topological invariants, the induced geometric space becomes unstable and 2D-to-3D lifting is ill-conditioned. Learning directly from high-dimensional observations without explicit structure is brittle and suffers from the curse of dimensionality [15]. Consequently, lifting predicted lanes to 3D can yield structural collapse in the reconstructed road space, manifesting as spurious concavities, bulges, and twists.

To preserve the metric and topological invariants of road space, we ground our formulation in principles of road geometric design [67], which enforce alignment continuity and gradual variation of curvature and grade. Consequently, despite global undulations, each local neighborhood of the roadway is well approximated by a smooth, nonsingular surface. Building on this observation, we posit the Road-Manifold Assumption: the roadway is a smooth, embedded two-dimensional manifold  $\mathcal{M} \subset \mathbb{R}^3$  admitting a smooth atlas of Euclidean charts, and lanes are smooth one-dimensional submanifolds  $\gamma \subset \mathcal{M}$  that inherit both local smoothness and global coherence from  $\mathcal{M}$ . Lane points are treated as sufficiently dense samples on these submanifolds. Equipped with the ambient Euclidean metric  $g$  restricted to  $\mathcal{M}$  by the pullback [12], the pair  $(\mathcal{M}, g)$  forms a Riemannian manifold [34] that provides intrinsic distances and enables coordinate-invariant objectives and regularizers. This representation supports principled dimensionality reduction [28] and facilitates learning and inference in a low-dimensional space while preserving geometric and topological fidelity. To encode intrinsic structural correlations on  $\mathcal{M}$ , we model local relationships in tangent spaces using symmetric positive definite (SPD) matrices, which are widely used in medical imaging [8, 14], signal processing [25, 27], and computer vision [11, 45, 46].

Although numerous neural networks on SPD manifolds (denoted by  $\text{Sym}_+^n$ ) [12, 32, 64–66, 77] have been proposed, many apply Riemannian operations without establishing or evaluating that the data admit a well-defined manifold structure. We make this requirement explicit via the Road-Manifold Assumption, which provides the geometric foundation of our approach. Building on this premise and leveraging visual cues, we introduce ReManNet, a Riemannian manifold network for monocular 3D lane detection that fuses visual features with geometric representations on  $\text{Sym}_+^n$ . Concretely, the network predicts raw 3D lane points using an image backbone and detection heads, then strengthens spatial relations using a position-weighted convolution layer. It estimates local SPD covariances [44] to construct Riemannian Gaussian [49] descriptors and aligns them via parallel transport [70] along geodesics induced by the affine-invariant Riemannian metric (AIRM) [23]. For numerically stable Euclidean processing, the descriptors are mapped to the Lie algebra via the matrix logarithm, vectorized, and projected to compact fusion features [50]. A gating module adaptively fuses the visual and geometric streams. For holistic supervision, we introduce the 3D Tunnel Lane IoU (3D-TLIoU) loss, which measures slice-wise overlap of tubular neighborhoods along each lane, providing shape-level guidance and improving metric accuracy.

Our contributions are summarized as follows:

- **Road-Manifold Assumption.** We introduce the Road-Manifold Assumption, which formalizes road space as a

smooth 2D manifold in  $\mathbb{R}^3$  with lane markings as 1D submanifolds and points as dense samples. This yields a consistent representation of metric and topological structure across road surfaces, lane curves, and sampled points.

- **ReManNet.** We propose a Riemannian manifold network that bootstraps image-based coordinate proposals, encodes lane geometry as Riemannian Gaussian descriptors on the  $\text{Sym}_+^n$ , enforces geodesic consistency via AIRM-based parallel transport, and fuses geometric descriptors with image features through a gating module to produce robust 3D lane predictions.
- **3D Tunnel Lane IoU (3D-TLIoU) Loss.** We introduce a slice-wise IoU between tubular neighborhoods swept along each lane, delivering holistic, shape-level supervision beyond conventional point-wise distance losses.
- **State-of-the-art performance.** ReManNet achieves leading results on standard benchmarks. On OpenLane, it improves the F1 score by +8.2% over the baseline and by +1.8% over the previous best, while achieving the best category accuracy and localization performance. In scene-level evaluations, it surpasses existing methods in most scenarios, with a maximum F1 gain of +6.6%.

## 2. Related Work

### 2.1. 3D Lane Detection

Estimating the 3D geometry of lanes is a fundamental task in autonomous driving, serving as a critical prerequisite for downstream navigation and planning [42, 69, 72]. A direct route is to acquire depth with specialized sensors [40, 55], but hardware cost and the maintenance burden of multi-sensor rigs hinder large-scale deployment. These constraints motivate monocular 3D lane detection, which infers 3D coordinates from a single RGB image.

In this setting, depth-guided regression first predicts a depth field and then recovers the 3D layout [19, 38, 52, 68]. For example, SALAD [68] performs 3D lane detection by jointly learning 2D semantic segmentation and monocular depth, then lifting the segmented lane evidence into 3D. However, because coordinate inference depends on an intermediate depth map, accuracy is fundamentally limited by depth quality, and errors propagate through the pipeline.

Another strand projects image features into BEV space [9, 17, 18, 36]. 3DLaneNet [17] applies inverse perspective mapping (IPM) to transform front-view (FV) features into BEV and regress BEV lane-anchor offsets. This pipeline tacitly assumes local planarity. Nonplanar geometry, such as ramps, undulating segments, and superelevated curves, systematically warps the BEV representation, propagating 2D feature distortions into 3D metric error.

Alternatively, some methods model lanes as structured line primitives, either through explicit parameterizations, including anchor templates [20, 21, 75], polynomial or

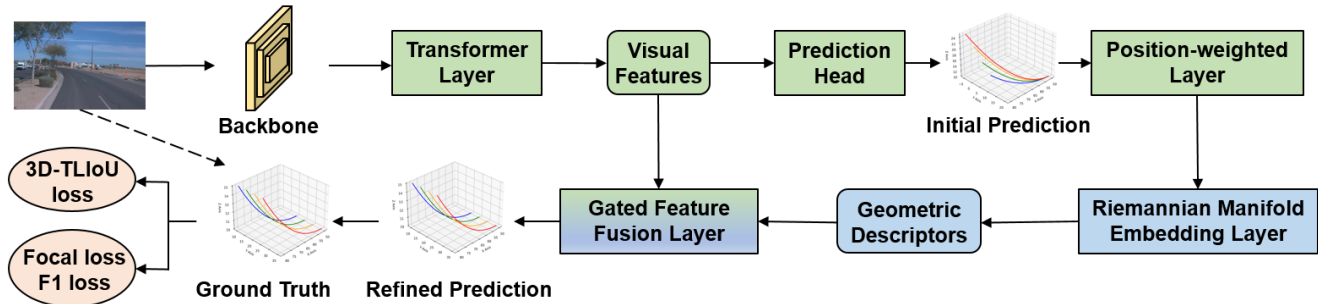


Figure 1. Overall architecture of ReManNet. A backbone and transformer generate initial lane predictions. A position-weighted layer encodes spatial context, and a Riemannian manifold embedding layer maps the resulting features to SPD Gaussian descriptors. A gated visual-geometric fusion layer combines these descriptors with visual features to produce refined predictions. The entire network is trained end-to-end using our geometry-consistent 3D-TLIoU loss alongside standard regression and classification objectives.

spline curves [4, 26, 52], and keypoint detection [48, 63] followed by polyline association. Anchor3DLane [20] projects anchors onto the FV feature to extract anchor-aligned features. LaneCPP [52] employs a B-spline parameterization for detection. GLane3D [48] detects lanes as a graph of keypoints. Many methods also introduce geometric priors such as nominal lane width [2], parallelism [20], and surface smoothness [52]. These priors can stabilize optimization, but they do not hold universally under lane additions, drops, variable widths, or sharp curvature transitions.

Reconstruction-centric [30, 39] and graph-optimization [48] methods serve as global formulations of geometric priors: they learn geometry-aware embeddings and enforce local connectivity, yet recover surfaces extrinsically in Euclidean space. The resulting geometry inherits a chordal Euclidean metric rather than the intrinsic geodesic metric on the road surface. This metric incompatibility precludes local isometry and curvature preservation, conflates geodesic neighborhoods with their Euclidean counterparts, and induces normal-direction smoothing akin to mean curvature flow. Thin structures consequently collapse, curvature estimates become biased, and spurious topological shortcuts emerge, degrading stability and physical interpretability.

## 2.2. Manifold Learning

Manifold learning addresses geometric representation and nonlinear dimensionality reduction by assuming that high-dimensional observations lie near a low-dimensional smooth manifold. The goal is to preserve intrinsic geometry such as distances and neighborhood relations, which mitigates the curse of dimensionality [15] and surpasses linear methods like Principal Component Analysis (PCA) [1, 60], Multidimensional Scaling (MDS) [13], and Linear Discriminant Analysis (LDA) [16]. Representative approaches include Isometric Feature Mapping (ISOMAP) [58], which preserves geodesic distances; Locally Linear Embedding (LLE) [53], which reconstructs each sample from its nearest

neighbors; and Laplacian Eigenmaps [6], which constructs a spectral embedding via the graph Laplacian.

Correlations in non-Euclidean data are naturally modeled on  $\text{Sym}_+^n$ . Equipped with Riemannian metrics such as AIRM [23], the Log-Euclidean metric (LEM) [3], and the Log Cholesky metric (LCM) [35], SPD geometry supplies geodesic distances and stable tangent-space operations. This supports learning that is globally nonlinear yet locally linear, and has proven effective in a range of tasks such as action recognition [44, 71], scene classification [57, 62], and facial emotion recognition [7, 22].

Within this framework, Gaussian embeddings provide principled summaries of local distributions, uncertainty, and correlations. In statistics and computer vision, they are used to compare distributions and build geometry-aware features. A prevalent strategy identifies Gaussian families with SPD matrices by endowing the covariance space with a Riemannian symmetric-space structure, yielding closed-form distances and tractable embeddings [37]. Related work connects Gaussians to subspaces of AIRM [23] and leverages Log-Euclidean geometry [3] for efficient linear embeddings in the log domain [31]. Beyond Euclidean domains, Gaussian models have been generalized to  $\text{Sym}_+^n$ , symmetric spaces [54], and homogeneous spaces [59].

These advances motivate the use of Riemannian Gaussians as intrinsic descriptors. They preserve coordinate invariance, capture anisotropy and correlation, and admit principled parallel transport on the manifold. In 3D lane detection, such descriptors summarize local neighborhoods in a way that respects the underlying geometry, enabling robust feature fusion and supporting coherent reasoning.

## 3. Method

### 3.1. Lane Representation

The goal of 3D lane detection is to predict a set of 3D lanes from a single input image  $\mathbf{I} \in \mathbb{R}^{3 \times H \times W}$ . We rep-

represent the lane set as  $\Omega = \{\mathbf{L}_j\}_{j=1}^K$ , where  $K$  is the number of lane instances. Each lane  $\mathbf{L}_j = (\mathbf{P}_j, C_j)$  consists of a category label  $C_j$  and a fixed-length point sequence  $\mathbf{P}_j = \{(x_i^j, y_i, z_i^j)\}_{i=1}^Q$ , where  $Q$  is the predefined number of sampled points. Following prior work [9, 18], the longitudinal coordinates are sampled from a predefined reference set  $Y_{\text{ref}} = \{y_i\}_{i=1}^Q$ , which is shared across all lanes.

## 3.2. Riemannian Manifold Neural Network

### 3.2.1. Method Overview

Figure 1 shows the overall architecture of ReManNet. Given an input image  $\mathbf{I} \in \mathbb{R}^{3 \times H \times W}$ , we first adopt an anchor-based pipeline [20] to obtain an initial set of lane predictions

$$\Omega^{(0)} = \{\mathbf{L}_j^{(0)} \mid j = 1, \dots, K\}, \quad \mathbf{L}_j^{(0)} = (\mathbf{P}_j^{(0)}, C_j^{(0)}), \quad (1)$$

where the initial 3D point sequence of lane  $j$  is

$$\mathbf{P}_j^{(0)} = \{(x_i^j, y_i, z_i^j)\}_{i=1}^Q, \quad \{y_i\}_{i=1}^Q \subset Y_{\text{ref}}. \quad (2)$$

We stack the initial lane point sequences into a tensor  $\mathbf{X}^{\text{in}} \in \mathbb{R}^{Q \times K \times 3}$ . Then feed it into a position-weighted convolutional encoder to extract compact geometric features. For the  $i$ -th sampled position on lane  $j$ , the position-weighted convolution is defined as

$$\mathbf{x}_{i,j}^{\text{out}} = \sum_{i' \in \mathcal{E}_i} \alpha_{i,i'}^{(j)} \widetilde{\mathbf{W}}_r \mathbf{x}_{i',j}^{\text{in}}, \quad r = i' - i \in \{-1, 0, +1\}, \quad (3)$$

where  $\mathcal{E}_i = \{i-1, i, i+1\}$  denotes the local neighborhood along lane  $j$ . The distance-aware weights are

$$\alpha_{i,i'}^{(j)} = \frac{\exp\left(-\frac{1}{\tau} |y_i^j - y_{i'}^j|\right)}{\sum_{k \in \mathcal{E}_i} \exp\left(-\frac{1}{\tau} |y_i^j - y_k^j|\right)}, \quad \sum_{i' \in \mathcal{E}_i} \alpha_{i,i'}^{(j)} = 1, \quad (4)$$

where  $\tau$  is a learnable temperature parameter. The relative-position kernel is

$$\widetilde{\mathbf{W}}_r = \begin{cases} \mathbf{W}_{-1}, & \text{if } r = -1, \\ \mathbf{W}_0, & \text{if } r = 0, \\ \mathbf{W}_{+1}, & \text{if } r = +1, \end{cases} \quad (5)$$

with learnable matrices  $\{\mathbf{W}_{-1}, \mathbf{W}_0, \mathbf{W}_{+1}\}$ .

Based on the encoded lane features, we perform k-means clustering and summarize each cluster with a Gaussian distribution. These Gaussians are then embedded into the SPD manifold through a diffeomorphic mapping [44], where we compute Riemannian statistics, including the manifold mean, tangent-space covariance, and transported local features [43, 49, 56, 70]. The resulting mean-covariance pairs serve as Riemannian Gaussian descriptors for local lane neighborhoods.

To integrate these descriptors into the network, we map

the SPD matrices to the Lie algebra using the matrix logarithm [61] and apply a learnable lower-triangular transform to obtain compact Euclidean features. A gated visual-geometric fusion module then combines these manifold features with image features, followed by classification and regression heads that produce the final predictions.

The following subsections detail the Riemannian-manifold modules built on the position-weighted encoder.

### 3.2.2. SPD Manifold Embedding of Gaussians

Let  $\mathbf{X}^{\text{out}} \in \mathbb{R}^{Q \times K \times d}$  denote the output of the position-weighted convolutional layer. It consists of  $Q \times K$  feature vectors in  $\mathbb{R}^d$ , which we partition into  $S$  groups by K-means,  $\mathbf{F}_s = \{\mathbf{f}_{s,m}\}_{m=1}^{q_s}$  for  $s = 1, \dots, S$ . Within each group, we model the features as approximately i.i.d. samples from a Gaussian  $\mathcal{N}(\boldsymbol{\mu}_s, \boldsymbol{\Sigma}_s)$ , capturing local feature consistency / local distributional regularity. The parameters are estimated by

$$\boldsymbol{\mu}_s = \frac{1}{q_s} \sum_{m=1}^{q_s} \mathbf{f}_{s,m}, \quad (6)$$

$$\boldsymbol{\Sigma}_s = \frac{1}{q_s - 1} \sum_{m=1}^{q_s} (\mathbf{f}_{s,m} - \boldsymbol{\mu}_s)(\mathbf{f}_{s,m} - \boldsymbol{\mu}_s)^\top. \quad (7)$$

Following the Gaussian-to-SPD construction in [44], we associate each Gaussian  $\mathcal{N}(\boldsymbol{\mu}_s, \boldsymbol{\Sigma}_s)$  with a unit-determinant SPD matrix

$$\mathbf{P}_s = (\det(\boldsymbol{\Sigma}_s))^{-\frac{1}{d+\rho}} \begin{bmatrix} \boldsymbol{\Sigma}_s + \rho \boldsymbol{\mu}_s \boldsymbol{\mu}_s^\top & \boldsymbol{\mu}_s^{(\rho)} \\ (\boldsymbol{\mu}_s^{(\rho)})^\top & \mathbf{I}_\rho \end{bmatrix}, \quad \boldsymbol{\mu}_s^{(\rho)} := \boldsymbol{\mu}_s \mathbf{1}_\rho^\top, \quad (8)$$

where  $\rho$  is a tunable embedding dimension,  $\mathbf{1}_\rho$  is a  $\rho$ -dimensional all-ones vector, and  $\mathbf{I}_\rho$  is the  $\rho \times \rho$  identity.  $\mathbf{P}_s$  has size  $(d + \rho) \times (d + \rho)$ .

By the Schur complement [47],

$$\det \begin{bmatrix} \boldsymbol{\Sigma}_s + \rho \boldsymbol{\mu}_s \boldsymbol{\mu}_s^\top & \boldsymbol{\mu}_s^{(\rho)} \\ (\boldsymbol{\mu}_s^{(\rho)})^\top & \mathbf{I}_\rho \end{bmatrix} = \det(\boldsymbol{\Sigma}_s). \quad (9)$$

Therefore, the scalar factor in Eq. (8) ensures that  $\det(\mathbf{P}_s) = 1$ , removing scale dependence. Moreover, since the corresponding Schur complement equals the covariance matrix  $\boldsymbol{\Sigma}_s \succ 0$ , the constructed matrix  $\mathbf{P}_s$  is positive definite, i.e.,  $\mathbf{P}_s \in \text{Sym}_+^{d+\rho}$ .

We implement (8) as a Gaussian embedding layer

$$\{\mathbf{P}_s\}_{s=1}^S = f_{\text{GaussEmbed}}(\{\mathbf{X}_{i,j}^{\text{out}}\}), \quad (10)$$

### 3.2.3. Gaussian Statistics on Riemannian Manifolds

**Riemannian Gaussian Statistics.** Let  $\{\mathbf{P}_s\}_{s=1}^S \subset \text{Sym}_+^n$  denote the SPD embeddings of feature groups. We aggregate these elements using the Riemannian mean under the AIRM [23]. The geodesic distance  $d_R(\cdot, \cdot)$  is

$$d_R(\mathbf{A}, \mathbf{B}) = \left\| \log(\mathbf{A}^{-1/2} \mathbf{B} \mathbf{A}^{-1/2}) \right\|_F, \quad (11)$$

For a candidate SPD point  $\mathbf{Y} \in \text{Sym}_+^n$ , the Riemannian mean is defined as

$$\mathbf{P}_m = \arg \min_{\mathbf{Y} \in \text{Sym}_+^n} \frac{1}{S} \sum_{s=1}^S d_R(\mathbf{Y}, \mathbf{P}_s)^2. \quad (12)$$

It can be computed by the standard log–average–exp iteration [43]

$$\mathbf{Y}^{(t+1)} = \text{Exp}_{\mathbf{Y}^{(t)}} \left( \frac{1}{S} \sum_{s=1}^S \text{Log}_{\mathbf{Y}^{(t)}}(\mathbf{P}_s) \right), \mathbf{P}_m = \lim_{t \rightarrow \infty} \mathbf{Y}^{(t)}, \quad (13)$$

where, under AIRM [23] and [50]

$$\text{Log}_{\mathbf{Y}}(\mathbf{P}) = \mathbf{Y}^{1/2} \log(\mathbf{Y}^{-1/2} \mathbf{P} \mathbf{Y}^{-1/2}) \mathbf{Y}^{1/2}, \quad (14)$$

$$\text{Exp}_{\mathbf{Y}}(\mathbf{X}) = \mathbf{Y}^{1/2} \exp(\mathbf{Y}^{-1/2} \mathbf{X} \mathbf{Y}^{-1/2}) \mathbf{Y}^{1/2}. \quad (15)$$

Let  $\mathbf{X}_s = \text{Log}_{\mathbf{P}_m}(\mathbf{P}_s) \in T_{\mathbf{P}_m} \text{Sym}_+^n$ . Map each symmetric  $\mathbf{X}_s$  to a Euclidean vector via the norm-preserving half-vectorization  $\text{svec}(\cdot)$  (off-diagonals scaled by  $\sqrt{2}$ ), i.e.,  $\mathbf{v}_s = \text{svec}(\mathbf{X}_s) \in \mathbb{R}^p$  with the dimension of the symmetric vectorization  $p = n(n+1)/2$ . The empirical covariance [49] is

$$\mathbf{P}_c = \frac{1}{S-1} \sum_{s=1}^S (\mathbf{v}_s - \bar{\mathbf{v}})(\mathbf{v}_s - \bar{\mathbf{v}})^\top, \bar{\mathbf{v}} = \frac{1}{S} \sum_{s=1}^S \mathbf{v}_s. \quad (16)$$

In practice, when  $S \leq p$  or for numerical stability, a small ridge  $\varepsilon \mathbf{I}_p$  can be added to ensure  $\mathbf{P}_c \in \text{Sym}_+^p$  before downstream operations.

**Parallel Transport.** To express tangent features in a unified coordinate system, we transport each tangent vector to an SPD reference  $\mathbf{P}_{\text{ref}}$ . Given  $\mathbf{X}_s = \text{Log}_{\mathbf{P}_m}(\mathbf{P}_s) \in T_{\mathbf{P}_m} \text{Sym}_+^n$ , we apply parallel transport [56, 70] along the AIRM geodesic from  $\mathbf{P}_m$  to  $\mathbf{P}_{\text{ref}}$ . Under AIRM, the transport admits the closed form

$$\tilde{\mathbf{X}}_s = \Gamma_{\mathbf{P}_m \rightarrow \mathbf{P}_{\text{ref}}}(\mathbf{X}_s) = \mathbf{C} \mathbf{X}_s \mathbf{C}^\top. \quad (17)$$

$$\begin{aligned} \mathbf{C} &= \mathbf{P}_{\text{ref}}^{1/2} (\mathbf{P}_{\text{ref}}^{-1/2} \mathbf{P}_m \mathbf{P}_{\text{ref}}^{-1/2})^{-1/2} \mathbf{P}_{\text{ref}}^{1/2} \\ &= \mathbf{P}_m^{1/2} (\mathbf{P}_m^{-1/2} \mathbf{P}_{\text{ref}} \mathbf{P}_m^{-1/2})^{1/2} \mathbf{P}_m^{-1/2}. \end{aligned} \quad (18)$$

**Riemannian Gaussian Statistics Layer.** Riemannian statistics aggregation is implemented as a network layer

$$\{\mathbf{P}_m, \mathbf{P}_c\} = f_{\text{RiemStats}}(\{\mathbf{P}_s\}_{s=1}^S, \mathbf{W}_{\text{pt}}), \quad (19)$$

where  $\mathbf{W}_{\text{pt}}$  parameterizes a learnable SPD reference  $\mathbf{P}_{\text{ref}}(\mathbf{W}_{\text{pt}})$ . The covariance is computed from transported tangent features by substituting the following  $\mathbf{v}_s$  to Eq. (16)

$$\mathbf{v}_s = \text{svec}(\mathcal{T}_{\mathbf{P}_m \rightarrow \mathbf{P}_{\text{ref}}}^{\mathbf{W}_{\text{pt}}}(\text{Log}_{\mathbf{P}_m} \mathbf{P}_s)), \quad (20)$$

where  $\mathcal{T}_{\mathbf{P}_m \rightarrow \mathbf{P}_{\text{ref}}}^{\mathbf{W}_{\text{pt}}}$  denotes the AIRM parallel transport from  $T_{\mathbf{P}_m} \text{Sym}_+^n$  to  $T_{\mathbf{P}_{\text{ref}}(\mathbf{W}_{\text{pt}})} \text{Sym}_+^n$ . This layer thus outputs the mean-covariance pair  $(\mathbf{P}_m, \mathbf{P}_c)$ .

### 3.2.4. Network Embedding of Riemannian Gaussians

Given the mean-covariance pair  $(\mathbf{P}_m, \mathbf{P}_c) \in \text{Sym}_+^n \times \text{Sym}_+^p$  computed from the Riemannian statistics layer in Eq. (19), we next map this descriptor to a manifold-aware Lie-group parameterization, which preserves its first- and second-order statistics while enabling stable Euclidean processing in the network.

The Riemannian mean channel is expressed in global coordinates through  $\zeta : \text{Sym}_+^n \rightarrow \mathbb{R}^p$ , with

$$\zeta(\mathbf{P}_m) = \text{svec}(\log \mathbf{P}_m), \quad \zeta^{-1}(u) = \exp(\text{smat}(u)), \quad (21)$$

where  $\text{svec}(\cdot)$  and  $\text{smat}(\cdot)$  denote symmetric vectorization and its inverse, respectively, with output dimension  $p = n(n+1)/2$ .

Writing the covariance as  $\mathbf{P}_c = \mathbf{L}\mathbf{L}^\top$  with  $\mathbf{L} \in \text{LT}_+^p$  (Cholesky factor [35]), where  $\text{LT}_+^p$  denotes the set of full-rank lower-triangular matrices with positive diagonal entries, we adopt a semidirect-product parameterization of the mean-covariance pair [44]:

$$\begin{aligned} (\mathbf{P}_1^m, \mathbf{P}_1^c) \star (\mathbf{P}_2^m, \mathbf{P}_2^c) &= \left( \zeta^{-1}(\mathbf{L}_2^\top \zeta(\mathbf{P}_1^m) + \zeta(\mathbf{P}_2^m)), \right. \\ &\quad \left. (\mathbf{L}_1 \mathbf{L}_2)(\mathbf{L}_1 \mathbf{L}_2)^\top \right), \end{aligned} \quad (22)$$

This formulation couples the mean coordinates and covariance factors in an associative form suitable for subsequent network embedding.

A concrete matrix realization is given by the block lower-triangular group

$$\mathcal{B}_p^+ = \left\{ \begin{bmatrix} \mathbf{L} & \mathbf{0} \\ \zeta(\mathbf{P}_m)^\top & 1 \end{bmatrix} \mid \mathbf{L} \in \text{LT}_+^p, \mathbf{P}_m \in \text{Sym}_+^n \right\} \quad (23)$$

Accordingly, we define the embedding layer as

$$\mathbf{G} = \begin{bmatrix} \mathbf{L} & \mathbf{0} \\ \zeta(\mathbf{P}_m)^\top & 1 \end{bmatrix}, \{\mathbf{G}\} = f_{\text{GroupEmbed}}(\{\mathbf{P}_m, \mathbf{P}_c\}) \quad (24)$$

This representation preserves manifold statistics while providing an algebraically convenient form for associative composition and stable Euclidean processing.

**Triangular Mapping and SPD Projection.** To obtain a compact descriptor for network fusion, we further apply a learnable lower-triangular transformation

$$\mathbf{D} = \mathbf{G} \mathbf{W}_\Delta, \quad \mathbf{W}_\Delta \in \text{LT}_+^{p+1} \text{ (diag} > 0). \quad (25)$$

where the positivity of the diagonal of  $\mathbf{W}_\Delta$  ensures that  $\mathbf{D}$  remains full-rank lower-triangular. We then project it back to the SPD cone by

$$\mathbf{Q} = \mathbf{D}\mathbf{D}^\top \in \text{Sym}_+^{p+1}. \quad (26)$$

Working in the log domain locally linearizes the AIRM ge-

ometry. We therefore compute

$$\mathbf{E} = \log(\mathbf{Q}), \quad \tilde{\mathbf{H}} = \text{svec}(\mathbf{E}) \in \mathbb{R}^{d_g}, \quad d_g = \frac{(p+1)(p+2)}{2}. \quad (27)$$

Since the raw SPD-log descriptor dimension  $d_g$  is determined by the manifold construction, we use a linear projection to obtain the final fusion descriptor:

$$\mathbf{H} = \phi_h(\tilde{\mathbf{H}}) = \tilde{\mathbf{H}}\mathbf{W}_h \in \mathbb{R}^{d_h}, \quad \mathbf{W}_h \in \mathbb{R}^{d_g \times d_h}. \quad (28)$$

The overall pipeline is implemented as

$$\{\mathbf{H}\} = f_{\text{SPDProj}}(f_{\text{TriMap}}(\mathbf{G}, \mathbf{W}_\Delta), \mathbf{W}_h). \quad (29)$$

### 3.2.5. Gated Visual–Geometric Feature Fusion

Let  $\mathbf{F}_{\text{anchor}} \in \mathbb{R}^{B \times A \times d_a}$  denote the anchor-level visual features from the initial prediction module, where  $B$  is the batch size,  $A$  is the anchor dimension of visual branch, and  $d_a$  is the visual feature dimension. Let  $\mathbf{H} \in \mathbb{R}^{B \times d_h}$  denote the geometric descriptor produced by Eq. (29). We broadcast  $\mathbf{H}$  along the anchor dimension so that all anchors of the same sample share the global geometric context:

$$\mathbf{H}_e = \text{expand}(\mathbf{H}) \in \mathbb{R}^{B \times A \times d_h}, \quad (30)$$

We then concatenate the visual and geometric features along the channel dimension:

$$\mathbf{Z} = \text{concat}(\mathbf{F}_{\text{anchor}}, \mathbf{H}_e) \in \mathbb{R}^{B \times A \times (d_a + d_h)}. \quad (31)$$

A per-anchor scalar gate is predicted from the concatenated feature:

$$\mathbf{s}_{\text{gate}} = \mathbf{Z}\mathbf{W}_{\text{gate}} \in \mathbb{R}^{B \times A \times 1}, \quad \mathbf{W}_{\text{gate}} \in \mathbb{R}^{(d_a + d_h) \times 1}. \quad (32)$$

To match the channel dimension of the geometric branch, we first project the visual anchor feature by

$$\mathbf{F}'_{\text{anchor}} = \mathbf{F}_{\text{anchor}}\mathbf{W}_a \in \mathbb{R}^{B \times A \times d_h}, \quad \mathbf{W}_a \in \mathbb{R}^{d_a \times d_h}. \quad (33)$$

With  $\mathbf{g} = \sigma(\mathbf{s}_{\text{gate}}) \in \mathbb{R}^{B \times A \times 1}$ , where  $\sigma(\cdot)$  is the element-wise sigmoid, the final fusion is formulated as an anchor-wise gated residual update:

$$\mathbf{F} = \mathbf{F}'_{\text{anchor}} + \mathbf{g} \odot \mathbf{H}_e \in \mathbb{R}^{B \times A \times d_h}, \quad (34)$$

where  $\odot$  denotes element-wise multiplication with broadcasting along the channel dimension. In this design, the visual anchor feature serves as the primary branch, whereas the geometric descriptor provides a gated residual correction for anchor-wise refinement. The fused feature  $\mathbf{F}$  is then routed to the subsequent classification and regression heads.

### 3.3. 3D Tunnel Lane IoU Loss

**Motivation.** Conventional point-wise distance losses score errors independently at sampled locations and thus underweight each sample’s contribution to global lane geometry. This makes optimization sensitive to local outliers and jitter, and encourages overfitting to point annotations. Moti-

vated by the LineIoU loss [74] for 2D lanes, we introduce the 3D Tunnel Lane IoU (3D-TLloU) loss, which measures the consistency between predicted and ground-truth tubular neighborhoods along the entire lane, thereby promoting shape-level alignment.

**Definition.** Sample each lane at  $Q$  slices along  $Y_{\text{ref}}$ . Let  $p_i = (x_i^p, z_i^p)$  and  $g_i = (x_i^g, z_i^g)$  denote the predicted and ground-truth points in the slice plane  $\{Y = Y_i\}$ , and set  $d_i = \|p_i - g_i\|$ . Given a tube radius  $r_{\text{tube}} > 0$ , we adopt a simple, monotone slice surrogate for the overlap between equal-radius disks

$$\widehat{\text{IoU}}_i = \frac{d_{\text{over}}}{d_{\text{union}}} = \frac{2r_{\text{tube}} - d_i}{2r_{\text{tube}} + d_i}, \quad (35)$$

where  $\widehat{\text{IoU}}_i$  can be negative to indicate the extent of separation between the two disks. To encode geometric coherence along the lane, define tangents  $\Delta p_i = p_i - p_{i-1}$  and  $\Delta g_i = g_i - g_{i-1}$  ( $i \geq 2$ ), the cosine similarity  $\text{Sim}_i = \frac{\Delta p_i^\top \Delta g_i}{\|\Delta p_i\| \|\Delta g_i\|}$ , and the associated penalty  $\mathcal{C}_i = \frac{1 - \text{Sim}_i}{2} \in [0, 1]$ .

Aggregating slice terms yields a curve-level objective that balances positional proximity and directional agreement. The 3D-TLloU loss is defined as

$$\mathcal{L}_{\text{3D-TLloU}} = 1 - \frac{\sum_{i=1}^Q (2r_{\text{tube}} - d_i)}{\sum_{i=1}^Q (2r_{\text{tube}} + d_i)} + \lambda_{\text{sim}} \frac{1}{Q-1} \sum_{i=2}^Q \mathcal{C}_i. \quad (36)$$

This formulation explicitly rewards overlap of tubular neighborhoods while regularizing tangent consistency, yielding robustness to small noise and improved geometric fidelity along the lane.

**Total loss.** The training objective combines classification, coordinate regression along  $x$  and  $z$ , and the proposed 3D-TLloU term

$$\mathcal{L}_{\text{total}} = \lambda_{\text{cls}} \mathcal{L}_{\text{cls}} + \lambda_{\text{reg}} (\mathcal{L}_x + \mathcal{L}_z) + \lambda_{\text{tliou}} \mathcal{L}_{\text{3D-TLloU}}. \quad (37)$$

Here,  $\lambda_{\text{cls}}$ ,  $\lambda_{\text{reg}}$ , and  $\lambda_{\text{tliou}}$  are the weights of the classification, regression, and 3D-TLloU losses, respectively.

## 4. Experiment

### 4.1. Datasets and Evaluation Metrics

**Datasets.** OpenLane [9] is a large-scale real-world benchmark for 3D lane detection built upon the Waymo Open Dataset. It contains 200K frames from 1,000 sequences at a resolution of  $1280 \times 1920$ , with over 880K lane annotations covering diverse weather, terrain, and lighting conditions. The benchmark provides per-frame camera intrinsics and extrinsics, and its annotations are comprehensive, including opposite-direction lanes without median barriers. In addition, OpenLane includes category and scene tags, and supports evaluation on a wide range of challenging scenarios, such as uphill and downhill roads, curves, extreme weather,

Method	Overall metrics						Scenario F1 (%)					
	F1 (%) $\uparrow$	Cate Acc (%) $\uparrow$	Ex/N (m) $\downarrow$	Ex/F (m) $\downarrow$	Ez/N (m) $\downarrow$	Ez/F (m) $\downarrow$	Up & Down $\uparrow$	Curve $\uparrow$	Extreme Weather $\uparrow$	Night $\uparrow$	Intersection $\uparrow$	Merge & Split $\uparrow$
3D-LaneNet [17] [CVPR2019]	44.1	–	0.479	0.572	0.367	0.443	40.8	46.5	47.5	41.5	32.1	41.7
GenLaneNet [18] [ECCV2020]	32.3	–	0.591	0.684	0.411	0.521	25.4	33.5	28.1	18.7	21.4	31.0
PersFormer [9] [ECCV2022]	50.5	92.3	0.485	0.553	0.364	0.431	42.4	55.6	48.6	46.6	40.0	50.7
CurveFormer [4] [ICRA2023]	50.5	–	0.340	0.772	0.207	0.651	45.2	56.6	49.7	49.1	42.9	45.4
LATR [39] [ICCV2023]	61.9	92.0	0.219	0.259	0.075	0.104	55.2	68.2	57.1	55.4	52.3	61.5
Anchor3DLane (R18) [20] [CVPR2023]	53.7	90.9	0.276	0.311	0.107	0.138	46.7	57.2	52.5	47.8	45.4	51.2
Anchor3DLane (R50) $\dagger$ [20] [CVPR2023]	57.5	91.6	0.233	0.246	0.080	0.106	52.7	60.8	56.2	54.7	49.8	56.0
LaneCPP [52] [CVPR2024]	60.3	–	0.264	0.310	0.077	0.117	53.6	64.4	56.7	54.9	52.0	58.7
PVALane (R50) [75] [AAAI2024]	62.7	–	0.232	0.259	0.092	0.118	54.1	67.3	62.0	57.2	53.4	60.0
Anchor3DLane++ (R18) [21] [TPAMI2024]	57.9	91.4	0.232	0.265	0.076	0.102	48.4	64.0	54.8	52.6	48.5	56.1
Anchor3DLane++ (R50) [21] [TPAMI2024]	62.4	93.4	0.202	0.237	0.073	0.100	54.1	68.4	58.3	55.4	53.1	61.1
MapTRv2 (R50) [33] [ICV2025]	53.6	88.9	0.267	0.312	0.074	0.105	50.0	53.2	54.9	51.3	43.1	53.1
Glane3D (R18) [48] [CVPR2025]	61.5	–	0.221	0.252	0.073	0.101	55.6	<b>69.1</b>	56.6	56.6	52.9	61.3
Glane3D (R50) [48] [CVPR2025]	63.9	–	0.193	0.234	0.065	0.090	58.2	71.1	60.1	60.2	55.0	<b>64.8</b>
ReManNet (R18) (Ours)	63.5	92.8	0.222	0.265	0.069	0.089	61.0	66.1	66.7	63.0	56.9	56.8
ReManNet (R50) (Ours)	<b>65.7</b>	<b>94.7</b>	<b>0.189</b>	<b>0.205</b>	<b>0.060</b>	<b>0.072</b>	<b>63.2</b>	67.9	<b>68.6</b>	<b>65.3</b>	<b>60.2</b>	59.9

Table 1. Comparison with SOTA methods on the OpenLane. The left block reports overall metrics: F1, category accuracy (Cate Acc), and mean  $x/z$  errors for the near (N) and far (F) ranges, denoted as  $\mathbf{Ex}/\mathbf{N}$ ,  $\mathbf{Ex}/\mathbf{F}$ ,  $\mathbf{Ez}/\mathbf{N}$ , and  $\mathbf{Ez}/\mathbf{F}$ . The right block reports scenario-wise F1. R18 and R50 denote ResNet-18 and ResNet-50 backbones;  $\dagger$  indicates the baseline. The best results are shown in **bold**.

Method	Balanced Scenes					Rare Subset					Visual Variations				
	F1 (%) $\uparrow$	Ex/N $\downarrow$	Ex/F $\downarrow$	Ez/N $\downarrow$	Ez/F $\downarrow$	F1 (%) $\uparrow$	Ex/N $\downarrow$	Ex/F $\downarrow$	Ez/N $\downarrow$	Ez/F $\downarrow$	F1 (%) $\uparrow$	Ex/N $\downarrow$	Ex/F $\downarrow$	Ez/N $\downarrow$	Ez/F $\downarrow$
3DLaneNet [17] [CVPR2019]	86.4	0.068	0.477	0.015	0.202	72.0	0.166	0.855	0.039	<b>0.521</b>	72.5	0.115	0.601	0.032	0.230
GenLaneNet [18] [ECCV2020]	88.1	0.061	0.496	0.012	0.214	78.0	0.139	0.903	0.030	0.539	85.3	0.074	0.538	0.015	0.232
CLGo [36] [AAAI2022]	91.9	0.061	0.361	0.029	0.250	86.1	0.147	0.735	0.071	0.609	87.3	0.084	0.464	0.045	0.312
PersFormer [9] [ECCV2022]	92.9	0.054	0.356	0.010	0.234	87.5	0.107	0.782	0.024	0.602	89.6	0.074	0.430	0.015	0.266
GP [30] [CVPR2022]	91.9	0.049	0.387	0.008	0.213	83.7	0.126	0.903	0.023	0.625	89.9	0.060	0.446	<b>0.011</b>	0.235
CurveFormer [4] [ICRA2023]	95.8	0.079	0.326	0.018	0.219	95.6	0.182	0.737	0.039	0.561	90.8	0.125	0.410	0.028	0.254
LATR [39] [ICCV2023]	96.8	0.022	0.253	<b>0.007</b>	<b>0.202</b>	96.1	0.050	0.600	<b>0.015</b>	0.532	95.1	0.045	0.315	0.016	0.228
Anchor3DLane $\dagger$ [20] [CVPR2023]	95.4	0.045	0.300	0.016	0.223	94.4	0.082	0.699	0.030	0.580	91.8	0.047	0.327	0.019	0.219
Anchor3DLane++ (R18) [21] [TPAMI2024]	96.3	0.027	0.268	0.011	0.215	96.4	0.050	0.617	0.019	0.551	92.7	0.045	0.371	0.019	0.250
Anchor3DLane++ (R50) [21] [TPAMI2024]	96.5	0.022	0.234	0.009	0.204	96.4	<b>0.043</b>	0.580	0.017	0.529	95.3	0.035	0.292	0.012	0.229
Glane3D [48] [CVPR2025]	<b>98.1</b>	<b>0.021</b>	0.250	0.007	0.213	<b>98.4</b>	0.044	0.621	0.023	0.566	92.7	0.046	0.364	0.020	0.317
ReManNet (R18) (Ours)	96.9	0.033	0.259	0.014	0.213	97.1	0.055	0.622	0.019	0.544	96.8	<b>0.033</b>	0.272	0.013	0.225
ReManNet (R50) (Ours)	96.9	0.035	<b>0.228</b>	0.020	<u>0.205</u>	97.2	0.055	<b>0.559</b>	0.030	<b>0.521</b>	<b>96.9</b>	0.034	<b>0.237</b>	<u>0.019</u>	<b>0.213</b>

Table 2. Comparison with SOTA methods on the ApolloSim. Results are reported on the **Balanced**, **Rare**, and **Visual Variations** subsets.  $\mathbf{Ex}/\mathbf{N}$ ,  $\mathbf{Ex}/\mathbf{F}$ ,  $\mathbf{Ez}/\mathbf{N}$ , and  $\mathbf{Ez}/\mathbf{F}$  denote mean  $x/z$  errors in the near (N) and far (F) ranges. R18 and R50 denote ResNet-18 and ResNet-50 backbones;  $\dagger$  indicates the baseline. The best and competitive results are highlighted in **bold** and underlined, respectively.

nighttime driving, intersections, and merge/split cases.

ApolloSim [18] is a photo-realistic synthetic benchmark built in the Unity 3D game engine. It contains 10,500 images spanning diverse virtual scenes (highway, urban, residential/downtown, rural) with variability in illumination, weather, traffic/obstacles, and road-surface quality. The dataset is organized into three subsets: Standard, Rare Scenes, and Visual Variations. It also provides per-frame camera parameters for 3D lane evaluation.

**Evaluation Metrics.** We follow the evaluation method of [20]: lanes are uniformly sampled along the longitudinal axis  $Y$  from 0 to 100 m. A predicted lane and a ground-truth lane are matched using a distance threshold  $\tau$  (we use 1.5 m here); a prediction is counted as a true positive if at

least 75% of its sampled points lie within  $\tau$  of the matched ground truth. We report the maximum F1 score under these criteria, together with mean lateral ( $x$ ) and vertical ( $z$ ) errors computed separately in the near (0–40 m) and far (40–100 m) ranges to assess geometric accuracy. On OpenLane, we also report category accuracy, defined as the proportion of true positives with correctly predicted categories.

## 4.2. Experimental Settings

We adopt Anchor3DLane [20] as our baseline and follow its anchor configuration. The number of sampled points per anchor is set to  $Q = 20$  on OpenLane and  $Q = 10$  on ApolloSim. All input images are resized to  $360 \times 480$ , and the backbone outputs feature maps of size  $45 \times 60 \times 64$ .

For module hyperparameters, the position-weighted convolutional layer produces  $d = 3$  channels. We apply  $k$ -means clustering with  $S = 30$  clusters and 20 iterations. The embedding dimension  $\rho$  in Eq. (8) is fixed to 1, and the geometric descriptor  $\mathbf{H}$  has dimension  $d_h = 256$ .

For loss functions, the 3D-TLlIoU tube radius is set to  $r_{\text{tube}} = 1.5$  m with cosine-similarity weight  $\lambda_{\text{sim}} = 0.4$ . The global loss weights are  $\lambda_{\text{cls}} = 1$ ,  $\lambda_{\text{reg}} = 1$ , and  $\lambda_{\text{tlou}} = 0.5$ . We train the model on OpenLane and ApolloSim for 60K and 50K iterations, respectively, using the AdanW optimizer (learning rate  $2 \times 10^{-4}$ , weight decay  $1 \times 10^{-4}$ ), with a batch size of 4 and 8 data-loader workers. All experiments are conducted on a single NVIDIA GeForce RTX 4090 GPU with an AMD EPYC 9654 CPU.

### 4.3. Main Results

**OpenLane.** Table 1 presents results on the OpenLane dataset. ReManNet with a ResNet-50 backbone achieves SOTA performance, improving F1 by **+8.2%** over the Anchor3DLane ResNet-50 baseline and by **+1.8%** over the previous best. It also achieves the highest category accuracy and the lowest localization errors along  $x$  and  $z$  in both near and far ranges. At the scenario level, ReManNet ranks first in most settings, with gains of **+6.6%** in *Extreme Weather*, **+5.2%** in *Intersection*, **+5.1%** in *Night*, and **+5.0%** in *Up & Down*. These scenes exhibit weak visual cues or strong geometric variability, and the gains highlight the effectiveness of coupling road-manifold geometric consistency with visual features for 3D reasoning. Performance on *Merge & Split* is lower, which may stem from complex topological interactions that locally violate manifold consistency.

**ApolloSim.** In Table 2, we report results on the ApolloSim benchmark. ReManNet (R50) delivers the most balanced overall localization performance across the three subsets, particularly in terms of far-range errors. It achieves the lowest far-range  $x$ -axis error (Ex/F) on all three subsets. Along the  $z$  axis, it attains the best far-range error (Ez/F) on *Visual Variations* and a tied-best result on *Rare*, while remaining competitive on *Balanced*. On the *Visual Variations* subset, ReManNet (R50) also achieves the best F1 score, improving by **+1.6%** over the previous best, together with clear reductions in far-range errors on both  $x$  and  $z$ . These results suggest that the proposed manifold-based geometric encoding strengthens spatial coherence and robustness under diverse appearance and illumination changes.

**Ablation Study.** To validate the effectiveness of ReManNet components, we conduct four ablation settings on OpenLane: the baseline, adding only the 3D-TLlIoU loss, adding only the Riemannian Gaussian module, and the full ReManNet model (Table 3). Introducing the 3D-TLlIoU loss yields a **+3.0%** F1 improvement by enforcing consistent overlap supervision along lane curves. Adding the Riemannian Gaussian module improves F1 by **+4.5%**, indicat-

Baseline	3D-TLlIoU Loss	Riemannian Gaussian	F1 (%) $\uparrow$
✓			57.5
✓	✓		60.5
✓		✓	62.0
✓	✓	✓	<b>65.7</b>

Table 3. Ablation study of ReManNet components.

Baseline	$C_i$	3D LIoU term	F1 (%) $\uparrow$
✓			57.5
✓	✓		58.6
✓		✓	59.9
✓	✓	✓	<b>60.5</b>

Table 4. Ablation study of the 3D-TLlIoU loss.

ing that encoding geometric descriptors on the SPD manifold enhances spatial reasoning stability. Combining both leads to a substantial **+8.2%** gain, surpassing the individual contributions and confirming their complementary synergy. The joint design allows ReManNet to capture intrinsic geometric consistency and maintain robust 3D reasoning under diverse visual conditions, leading to the strongest performance among the ablated variants

For the 3D-TLlIoU loss, we ablate its two components, namely the cosine-similarity penalty  $C_i$  and the 3D LIoU term computed between predictions and ground truth. As shown in Table 4, adding  $C_i$  raises F1 from 57.5% to 58.6% (**+1.1%**), while using only 3D LIoU yields 59.9% (**+2.4%**). Combining both terms (full 3D-TLlIoU Loss) attains 60.5% (**+3.0%** over baseline), outperforming the  $C_i$ -only and LIoU-only variants by +1.9% and +0.6%. These gains indicate that  $C_i$  (directional alignment) and 3D LIoU (geometric overlap) are complementary and mutually reinforcing, yielding consistent improvements when combined.

## 5. Conclusion

In this work, we introduce the Road-Manifold Assumption to address geometric collapse when reconstructing road surfaces from lane predictions, a problem caused by the lack of intrinsic metric invariance in Euclidean space. Based on this assumption, we build an intrinsically consistent representation that aligns metric and topological structure across road surface, lane curves, and sampled points. We propose ReManNet, a Riemannian manifold network that fuses Riemannian Gaussian descriptors with visual features, alongside a geometry-consistent 3D-TLlIoU loss for supervision. Experiments on standard benchmarks demonstrate robust and accurate 3D lane detection with consistent gains over prior methods. Beyond lane detection, we hope this formulation and supervision strategy will inspire geometry-aware 3D perception, spatial reconstruction, and scene generation.

## 6. Acknowledgment

This work was supported by the Department of Science and Technology of Hubei Province under Grant 2023BAB146.

## References

- [1] Hervé Abdi and Lynne J Williams. Principal component analysis. *Wiley Interdisciplinary Reviews: Computational Statistics*, 2(4):433–459, 2010. 3
- [2] Jianyong Ai, Wenbo Ding, Jiu-Yang Zhao, and Jiachen Zhong. Ws-3d-lane: Weakly supervised 3d lane detection with 2d lane labels. In *IEEE International Conference on Robotics and Automation*, pages 5595–5601, 2023. 3
- [3] Vincent Arsigny, Pierre Fillard, Xavier Pennec, and Nicholas Ayache. *Fast and Simple Computations on Tensors with Log-Euclidean Metrics*. PhD thesis, Inria, 2005. 3
- [4] Yifeng Bai, Zhirong Chen, Zhangjie Fu, Lang Peng, Pengpeng Liang, and Erkang Cheng. Curveformer: 3d lane detection by curve propagation with curve queries and attention. In *IEEE International Conference on Robotics and Automation*, pages 7062–7068, 2023. 1, 3, 7
- [5] Yifeng Bai, Zhirong Chen, Pengpeng Liang, Bo Song, and Erkang Cheng. Curveformer++: 3d lane detection by curve propagation with temporal curve queries and attention. *IEEE Transactions on Intelligent Transportation Systems*, 2025. 1
- [6] Mikhail Belkin and Partha Niyogi. Laplacian eigenmaps for dimensionality reduction and data representation. *Neural Computation*, 15(6):1373–1396, 2003. 3
- [7] Daniel Brooks, Olivier Schwander, Frédéric Barbaresco, Jean-Yves Schneider, and Matthieu Cord. Riemannian batch normalization for spd neural networks. *Advances in Neural Information Processing Systems*, 32, 2019. 3
- [8] Rudrasis Chakraborty, Jose Bouza, Jonathan H. Manton, and Baba C. Vemuri. Manifoldnet: A deep neural network for manifold-valued data with applications. *IEEE Transactions on Pattern Analysis and Machine Intelligence*, 44(2):799–810, 2022. 2
- [9] Li Chen, Chonghao Sima, Yang Li, Zehan Zheng, Jiajie Xu, Xiangwei Geng, Hongyang Li, Conghui He, Jianping Shi, Yu Qiao, et al. Persformer: 3d lane detection via perspective transformer and the openlane benchmark. In *European Conference on Computer Vision*, pages 550–567. Springer, 2022. 1, 2, 4, 6, 7
- [10] Zhilu Chen and Xinming Huang. End-to-end learning for lane keeping of self-driving cars. In *IEEE Intelligent Vehicles Symposium*, pages 1856–1860. IEEE, 2017. 1
- [11] Ziheng Chen, Tianyang Xu, Xiao-Jun Wu, Rui Wang, Zhiwu Huang, and Josef Kittler. Riemannian local mechanism for spd neural networks. In *Proceedings of the AAAI Conference on Artificial Intelligence*, pages 7104–7112, 2023. 2
- [12] Ziheng Chen, Yue Song, Tianyang Xu, Zhiwu Huang, Xiao-Jun Wu, and Nicu Sebe. Adaptive log-euclidean metrics for spd matrix learning. *IEEE Transactions on Image Processing*, 2024. 2
- [13] Michael AA Cox and Trevor F Cox. Multidimensional scaling. In *Handbook of Data Visualization*, pages 315–347. Springer, 2008. 3
- [14] Asha Das, Madhu S. Nair, and S. David Peter. Sparse representation over learned dictionaries on the riemannian manifold for automated grading of nuclear pleomorphism in breast cancer. *IEEE Transactions on Image Processing*, 28(3):1248–1260, 2019. 2
- [15] David L Donoho et al. High-dimensional data analysis: The curses and blessings of dimensionality. *AMS math challenges lecture*, 1(2000):32, 2000. 1, 3
- [16] Richard O Duda, Peter E Hart, et al. *Pattern Classification*. John Wiley & Sons, 2006. 3
- [17] Noa Garnett, Rafi Cohen, Tomer Pe’er, Roei Lahav, and Dan Levi. 3d-lanenet: end-to-end 3d multiple lane detection. In *Proceedings of the IEEE/CVF International Conference on Computer Vision*, pages 2921–2930, 2019. 1, 2, 7
- [18] Yuliang Guo, Guang Chen, Peitao Zhao, Weide Zhang, Jinghao Miao, Jingao Wang, and Tae Eun Choe. Gen-lanenet: A generalized and scalable approach for 3d lane detection. In *European Conference on Computer Vision*, pages 666–681. Springer, 2020. 1, 2, 4, 7
- [19] Kuan-Chih Huang, Tsung-Han Wu, Hung-Ting Su, and Winston H Hsu. Monodtr: Monocular 3d object detection with depth-aware transformer. In *Proceedings of the IEEE/CVF Conference on Computer Vision and Pattern Recognition*, pages 4012–4021, 2022. 1, 2
- [20] Shaofei Huang, Zhenwei Shen, Zehao Huang, Zi-han Ding, Jiao Dai, Jizhong Han, Naiyan Wang, and Si Liu. Anchor3dlane: Learning to regress 3d anchors for monocular 3d lane detection. In *Proceedings of the IEEE/CVF Conference on Computer Vision and Pattern Recognition*, pages 17451–17460, 2023. 1, 2, 3, 4, 7
- [21] Shaofei Huang, Zhenwei Shen, Zehao Huang, Yue Liao, Jizhong Han, Naiyan Wang, and Si Liu. Anchor3dlane++: 3d lane detection via sample-adaptive sparse 3d anchor regression. *IEEE Transactions on Pattern Analysis and Machine Intelligence*, 2024. 1, 2, 7
- [22] Zhiwu Huang and Luc Van Gool. A riemannian network for spd matrix learning. In *Proceedings of the AAAI Conference on Artificial Intelligence*, 2017. 3
- [23] Ioana Ilea, Lionel Bombrun, Salem Said, and Yannick Berthoumieu. Covariance matrices encoding based on the log-euclidean and affine invariant riemannian metrics. In *Proceedings of the IEEE Conference on Computer Vision and Pattern Recognition Workshops*, pages 393–402, 2018. 2, 3, 4, 5
- [24] Shoucai Jing, Yao Feng, Fei Hui, Jianbei Liu, Xiangmo Zhao, and Asad J. Khattak. Efficient and eco lane-changing trajectory planning for connected and automated vehicles: Deep reinforcement learning-based method. *IEEE Transactions on Intelligent Transportation Systems*, 26(7):9882–9892, 2025. 1
- [25] Ce Ju, Reinmar J Kobler, Liyao Tang, Cuntai Guan, and Motoaki Kawanabe. Deep geodesic canonical correlation analysis for covariance-based neuroimaging data. In *The Twelfth International Conference on Learning Representations*, 2024. 2
- [26] Muhammet Esat Kalfaoglu, Halil Ibrahim Ozturk, Ozsel Kilinc, and Alptekin Temizel. Topobda: Towards bezier de-

- formable attention for road topology understanding. *Neuro-computing*, page 132360, 2025. 1, 3
- [27] Reinmar Kobler, Jun-ichiro Hirayama, Qibin Zhao, and Motoaki Kawanabe. Spd domain-specific batch normalization to crack interpretable unsupervised domain adaptation in eeg. *Advances in Neural Information Processing Systems*, 35: 6219–6235, 2022. 2
- [28] Martin HC Law and Anil K Jain. Incremental nonlinear dimensionality reduction by manifold learning. *IEEE Transactions on Pattern Analysis and Machine Intelligence*, 28(3): 377–391, 2006. 2
- [29] Der-Hau Lee. Lane-keeping control of autonomous vehicles through a soft-constrained iterative lqr. *IEEE Transactions on Vehicular Technology*, 74(4):5610–5623, 2025. 1
- [30] Chenguang Li, Jia Shi, Ya Wang, and Guangliang Cheng. Reconstruct from top view: A 3d lane detection approach based on geometry structure prior. In *Proceedings of the IEEE/CVF Conference on Computer Vision and Pattern Recognition*, pages 4370–4379, 2022. 1, 3, 7
- [31] Peihua Li, Qilong Wang, Hui Zeng, and Lei Zhang. Local log-euclidean multivariate gaussian descriptor and its application to image classification. *IEEE Transactions on Pattern Analysis and Machine Intelligence*, 39(4):803–817, 2016. 3
- [32] Yunchen Li, Zhou Yu, Gaoqi He, Yunhang Shen, Ke Li, Xing Sun, and Shaohui Lin. Spd-ddpm: Denoising diffusion probabilistic models in the symmetric positive definite space. In *Proceedings of the AAAI Conference on Artificial Intelligence*, pages 13709–13717, 2024. 2
- [33] Bencheng Liao, Shaoyu Chen, Yunchi Zhang, Bo Jiang, Qian Zhang, Wenyu Liu, Chang Huang, and Xinggang Wang. Maptrv2: An end-to-end framework for online vectorized hd map construction. *International Journal of Computer Vision*, 133(3):1352–1374, 2025. 7
- [34] Tong Lin and Hongbin Zha. Riemannian manifold learning. *IEEE Transactions on Pattern Analysis and Machine Intelligence*, 30(5):796–809, 2008. 2
- [35] Zhenhua Lin. Riemannian geometry of symmetric positive definite matrices via cholesky decomposition. *SIAM Journal on Matrix Analysis and Applications*, 40(4):1353–1370, 2019. 3, 5
- [36] Ruijin Liu, Dapeng Chen, Tie Liu, Zhiliang Xiong, and Zejian Yuan. Learning to predict 3d lane shape and camera pose from a single image via geometry constraints. In *Proceedings of the AAAI Conference on Artificial Intelligence*, pages 1765–1772, 2022. 1, 2, 7
- [37] Miroslav Lovrić, Maung Min-Oo, and Ernst A Ruh. Multivariate normal distributions parametrized as a riemannian symmetric space. *Journal of Multivariate Analysis*, 74(1): 36–48, 2000. 3
- [38] Yueru Luo, Xu Yan, Chaoda Zheng, Chao Zheng, Shuqi Mei, Tang Kun, Shuguang Cui, and Zhen Li. M 2-3dlanenet: Exploring multi-modal 3d lane detection. *arXiv preprint arXiv:2209.05996*, 2022. 1, 2
- [39] Yueru Luo, Chaoda Zheng, Xu Yan, Tang Kun, Chao Zheng, Shuguang Cui, and Zhen Li. Latr: 3d lane detection from monocular images with transformer. In *Proceedings of the IEEE/CVF International Conference on Computer Vision*, pages 7941–7952, 2023. 3, 7
- [40] Yueru Luo, Shuguang Cui, and Zhen Li. DV-3DLane: End-to-end multi-modal 3d lane detection with dual-view representation. In *The Twelfth International Conference on Learning Representations*, 2024. 2
- [41] Changsheng Lv, Mengshi Qi, Liang Liu, and Huadong Ma. T2sg: Traffic topology scene graph for topology reasoning in autonomous driving. In *Proceedings of the IEEE/CVF Conference on Computer Vision and Pattern Recognition*, pages 17197–17206, 2025. 1
- [42] Zhenqiang Ma, Hongjuan Zhang, Chengzhi Hong, Si Xu, Disheng Zhang, Jian Zhou, Zhijun Chen, and Bijun Li. Modeling of driving risk fields considering vehicle-lane interactions and its application in car-following model. *Physica A: Statistical Mechanics and its Applications*, page 131086, 2025. 2
- [43] Maher Moakher. A differentiable geometric approach to the geometric mean of symmetric positive-definite matrices. *SIAM Journal on Matrix Analysis and Applications*, 26(3): 735–747, 2005. 4, 5
- [44] Xuan Son Nguyen. Geomnet: A neural network based on riemannian geometries of spd matrix space and cholesky space for 3d skeleton-based interaction recognition. In *Proceedings of the IEEE/CVF International Conference on Computer Vision*, pages 13379–13389, 2021. 2, 3, 4, 5
- [45] Xuan Son Nguyen, Luc Brun, Olivier Lézoray, and Sébastien Boudoux. A neural network based on spd manifold learning for skeleton-based hand gesture recognition. In *Proceedings of the IEEE/CVF Conference on Computer Vision and Pattern Recognition*, pages 12036–12045, 2019. 2
- [46] Xuan Son Nguyen, Shuo Yang, and Aymeric Histace. Neural networks on symmetric spaces of noncompact type. In *The Thirteenth International Conference on Learning Representations*, 2025. 2
- [47] Diane Valerie Ouellette. Schur complements and statistics. *Linear Algebra and its Applications*, 36:187–295, 1981. 4
- [48] Halil İbrahim Öztürk, Muhammet Esat Kalfaoğlu, and Ozsel Kilinc. Glane3d: Detecting lanes with graph of 3d keypoints. In *Proceedings of the IEEE/CVF Conference on Computer Vision and Pattern Recognition*, pages 27508–27518, 2025. 1, 3, 7
- [49] Xavier Pennec. *Probabilities and statistics on riemannian manifolds: A geometric approach*. PhD thesis, INRIA, 2004. 2, 4, 5
- [50] Xavier Pennec, Pierre Fillard, and Nicholas Ayache. A riemannian framework for tensor computing. *International Journal of Computer Vision*, 66(1):41–66, 2006. 2, 5
- [51] Maximilian Pittner, Alexandru Condurache, and Joel Janai. 3d-splinet: 3d traffic line detection using parametric spline representations. In *Proceedings of the IEEE/CVF Winter Conference on Applications of Computer Vision*, pages 602–611, 2023. 1
- [52] Maximilian Pittner, Joel Janai, and Alexandru P Condurache. Lanecpp: Continuous 3d lane detection using physical priors. In *Proceedings of the IEEE/CVF Conference on Computer Vision and Pattern Recognition*, pages 10639–10648, 2024. 1, 2, 3, 7

- [53] Sam T Roweis and Lawrence K Saul. Nonlinear dimensionality reduction by locally linear embedding. *Science*, 290(5500):2323–2326, 2000. 3
- [54] Salem Said, Lionel Bombrun, Yannick Berthoumieu, and Jonathan H Manton. Riemannian gaussian distributions on the space of symmetric positive definite matrices. *IEEE Transactions on Information Theory*, 63(4):2153–2170, 2017. 3
- [55] Yongchao Song, Jiping Bi, Lijun Sun, Zhaowei Liu, Yahong Jiang, and Xuan Wang. Freq-3dlane: 3d lane detection from monocular images via frequency-aware feature fusion. *IEEE Transactions on Intelligent Transportation Systems*, 2025. 2
- [56] Suvrit Sra and Reshad Hosseini. Conic geometric optimization on the manifold of positive definite matrices. *SIAM Journal on Optimization*, 25(1):713–739, 2015. 4, 5
- [57] Haoliang Sun, Xiantong Zhen, Yuanjie Zheng, Gongping Yang, Yilong Yin, and Shuo Li. Learning deep match kernels for image-set classification. In *Proceedings of the IEEE Conference on Computer Vision and Pattern Recognition*, pages 3307–3316, 2017. 3
- [58] Joshua B Tenenbaum, Vin de Silva, and John C Langford. A global geometric framework for nonlinear dimensionality reduction. *Science*, 290(5500):2319–2323, 2000. 3
- [59] Pavan Turaga, Ashok Veeraraghavan, and Rama Chellappa. Statistical analysis on stiefel and grassmann manifolds with applications in computer vision. In *Proceedings of the IEEE Conference on Computer Vision and Pattern Recognition*, pages 1–8. IEEE, 2008. 3
- [60] Matthew Turk and Alex Pentland. Eigenfaces for recognition. *Journal of Cognitive Neuroscience*, 3(1):71–86, 1991. 3
- [61] Raviteja Vemulapalli, Felipe Arrate, and Rama Chellappa. Human action recognition by representing 3d skeletons as points in a lie group. In *Proceedings of the IEEE Conference on computer vision and Pattern Recognition*, pages 588–595, 2014. 4
- [62] Rui Wang, Xiao-Jun Wu, and Josef Kittler. Symnet: A simple symmetric positive definite manifold deep learning method for image set classification. *IEEE Transactions on Neural Networks and Learning Systems*, 33(5):2208–2222, 2021. 3
- [63] Ruihao Wang, Jian Qin, Kaiying Li, Yaochen Li, Dong Cao, and Jintao Xu. Bev-lanedet: An efficient 3d lane detection based on virtual camera via key-points. In *Proceedings of the IEEE/CVF Conference on Computer Vision and Pattern Recognition*, pages 1002–1011, 2023. 1, 3
- [64] Rui Wang, Xiao-Jun Wu, Ziheng Chen, Cong Hu, and Josef Kittler. Spd manifold deep metric learning for image set classification. *IEEE Transactions on Neural Networks and Learning Systems*, 35(7):8924–8938, 2024. 2
- [65] Rui Wang, Shaocheng Jin, Zhenyu Cai, Ziheng Chen, Xiao-Jun Wu, and Josef Kittler. Learning a better spd network for signal classification: A riemannian batch normalization method. *IEEE Transactions on Neural Networks and Learning Systems*, 2025.
- [66] Rui Wang, Shaocheng Jin, Ziheng Chen, Xiaoqing Luo, and Xiao-Jun Wu. Learning to normalize on the spd manifold under bures-wasserstein geometry. In *Proceedings of the IEEE/CVF Conference on Computer Vision and Pattern Recognition*, pages 8289–8298, 2025. 2
- [67] Keith Wollhuter. *Geometric Design of Roads Handbook*. CRC Press, 2015. 2
- [68] Fan Yan, Ming Nie, Xinyue Cai, Jianhua Han, Hang Xu, Zhen Yang, Chaoqiang Ye, Yanwei Fu, Michael Bi Mi, and Li Zhang. Once-3dlanes: Building monocular 3d lane detection. In *Proceedings of the IEEE/CVF Conference on Computer Vision and Pattern Recognition*, pages 17143–17152, 2022. 1, 2
- [69] Hongjuan Zhang, Chuang Qian, Wenzhuo Li, and Bijun Li. A vision-aided rtk ambiguity resolution method by map lane matching for intelligent vehicle in urban environment. *International Journal of Digital Earth*, 17(1):2383479, 2024. 2
- [70] Miaomiao Zhang and Tom Fletcher. Probabilistic principal geodesic analysis. *Advances in Neural Information Processing Systems*, 26, 2013. 2, 4, 5
- [71] Tong Zhang, Wenming Zheng, Zhen Cui, Yuan Zong, Chaolong Li, Xiaoyan Zhou, and Jian Yang. Deep manifold-to-manifold transforming network for skeleton-based action recognition. *IEEE Transactions on Multimedia*, 22(11):2926–2937, 2020. 3
- [72] Ling Zheng, Chengzhi Hong, Huashan Song, and Rong Chen. An autonomous mobile robot path planning strategy using an enhanced slime mold algorithm. *Frontiers in Neurobotics*, 17:1270860, 2023. 2
- [73] Ling Zheng, Yan Tian, Hu Wang, Chengzhi Hong, and Bijun Li. Path planning of autonomous mobile robots based on an improved slime mould algorithm. *Drones*, 7(4):257, 2023. 1
- [74] Tu Zheng, Yifei Huang, Yang Liu, Wenjian Tang, Zheng Yang, Deng Cai, and Xiaofei He. Clrnet: Cross layer refinement network for lane detection. In *Proceedings of the IEEE/CVF Conference on Computer Vision and Pattern Recognition*, pages 898–907, 2022. 6
- [75] Zewen Zheng, Xuemin Zhang, Yongqiang Mou, Xiang Gao, Chengxin Li, Guoheng Huang, Chi-Man Pun, and Xiaochen Yuan. Pvalane: Prior-guided 3d lane detection with view-agnostic feature alignment. In *Proceedings of the AAAI Conference on Artificial Intelligence*, pages 7597–7604, 2024. 1, 2, 7
- [76] Meixia Zhi, Chen Deng, Bijun Li, Hongjuan Zhang, and Chengzhi Hong. A dynamic visual-inertial-wheel odometry with semantic constraints and denoised imu-odometer prior for autonomous driving. *IEEE Sensors Journal*, 24(17):27966–27980, 2024. 1
- [77] Xinxin Zou, Hao Xu, and Xinling Liu. Manifold learning based on locally linear embedding for symmetric positive definite matrix. *Pattern Recognition*, page 112691, 2025. 2